ADVANCED MATERIALS
www.advmat.de

Customized Enhancement of Thermal Sensitivity of Tumors at Different Subcutaneous Depths by Multichannel Lanthanide Nanocomposites

Yuxin Liu, Zheng Wei, Jieying Zhang, Yang Xu, Jing Zhou, Zhanfang Ma, Francesco G. Mutti, Hong Zhang, Xingjun Zhu,* and Felix F. Loeffler**

The photothermal therapeutic effect on tumors located at different subcutaneous depths varies due to the attenuation of light by tissue. Here, based on the wavelength-dependent optical attenuation properties of tissues, the tumor depth is assessed using a multichannel lanthanide nanocomposite. A zeolitic imidazolate framework (ZIF-8)-coated nanocomposite is able to deliver high amounts of the hydrophilic heat shock protein 90 inhibitor epigallocatechin gallate through a hydrogen-bonding network formed by the encapsulated highly polarized polyoxometalate guest. It is superior to both bare and PEGylated ZIF-8 for drug delivery. With the assessment of tumor depth and accumulated amount of nanocomposite by fluorescence, an irradiation prescription can be customized to release sufficient HSP90 inhibitor and generate heat for sensitized photothermal treatment of tumors, which not only ensured therapeutic efficacy but also minimized damage to the surrounding tissues.

1. Introduction

Photothermal therapy is an advanced and precise strategy for the treatment of tumors.[1] Photogenerated hyperthermia disrupts the structure of biomacromolecules, deactivates their functions, and thereby inhibits the growth of tumor cells. In a certain temperature range (≈42–45 °C), photothermal treatment can selectively induce apoptosis of tumor cells with little damage to neighboring healthy tissue.[2,3] In recent years, many photothermal conversion nanomedicines have been developed for effective treatment of subcutaneous tumors,[4–6] while our recently introduced customization strategy further improved the therapeutic precision.[7] Therefore, photothermal therapy is poised to be an alternative remedy for cancer. However, in real cancer cases, tumors are located in the subcutaneous tissue at different depths. Due to the attenuation by tissues, the penetration of excitation light is limited, and thus it becomes increasingly difficult to generate sufficient heat for treatment with increasing depth. As a result, the therapeutic efficacy of photothermal treatment is different for tumors at different depths, and especially ineffective for deep-seated tumors.

To realize photothermal tumor treatment in deep tissues, the straightforward way is to use more intense excitation light, but this will cause damage to surrounding normal tissues and increase the risk of overtreatment. In contrast, reducing the tumor's resistance to heat should be a safer option. Hyperthermia stimulates cells to produce heat shock proteins (HSPs), which act as molecular chaperones to support biological processes (e.g., peptide folding and protein trafficking) to protect cells from heat stress.[8–10] As stress-inducible proteins, HSPs are also important regulators of the apoptotic pathway and contribute

Y. Liu, F. F. Loeffler
Department of Biomolecular Systems
Max Planck Institute of Colloids and Interfaces
14476 Potsdam, Germany
E-mail: Felix.Loeffler@mpikg.mpg.de
Y. Liu, Z. Wei, F. G. Mutti, H. Zhang
Van' t Hoff Institute for Molecular Sciences
Molecular Photonics & HIMS-Biocat, University of Amsterdam
Amsterdam 1098 XH, The Netherlands
E-mail: H.Zhang@uva.nl
The ORCID identification number(s) for the author(s) of this article can be found under https://doi.org/10.1002/adma.202402981

DOI: 10.1002/adma.202402981

Y. Liu
Institute of Chemistry and Biochemistry
Free University of Berlin
14195 Berlin, Germany
J. Zhang, X. Zhu
School of Physical Science and Technology & State Key Laboratory of Advanced Medical Materials and Devices
Shanghai Tech University
Shanghai 201210, China
E-mail: zhuxj1@shanghaitech.edu.cn
Y. Xu, J. Zhou, Z. Ma
Beijing Key Laboratory for Optical Materials and Photonic Devices
Capital Normal University
Beijing 100048, China

to therapeutic resistance and tumor cell survival.[11,12] HSP90 is one of the most abundant HSPs. Together with other chaperones, HSP90 promotes the folding and maturation of various proteins, as well as regulates various biological processes such as gene expression, cell cycle, and proliferation.[13] Its expression in tumor cells is higher than in normal cells, which can protect tumor cells and weaken the effect of photothermal therapy. Therefore, the use of HSP90 inhibitors may improve the sensitivity of tumor cells to hyperthermia and, in combination with photothermal conversion, nanomedicines may allow the treatment of deep-seated tumors.

However, in real cancer cases, tumors are located at different subcutaneous depths, causing large differences in photothermally induced temperatures due to varying light absorption and scattering. This could be adjusted by giving different dosages of HSP90 inhibitor. Therefore, there is a need for nanomedicines that can enable the assessment tumor depth to customize HSP90 release and ensure both high treatment efficacy and low side effects. Our recent approaches using multichannel lanthanide nanocomposites are expected to address this need.[14–16] Due to the unique optical properties of lanthanides, multichannel lanthanide nanocomposites have multiple independent signal channels and can therefore be used orthogonally for different functions.[17–21] In our recent work, we have simultaneously evaluated the tumor microenvironment and tailored the release of chemotherapeutics with multichannel lanthanide nanocomposites.[22] This may also be used to assess tumor depth and customize the release of HSP inhibitors.

Herein, a strategy for customized tumor sensitization in response to different photo-induced hyperthermia conditions at different tumor depths is proposed, using rationally designed multichannel lanthanide nanocomposites with a zeolitic imidazolate framework, $NaLuF_4$:Yb,Er,Tm@$NaLuF_4$@ZIF-8⊂reduced phosphomolybdate (Ln-ZIF⊂rPMo). Instead of in situ growth[23–25] the rPMo clusters are modified on the lanthanide-doped nanoparticle through a host–guest interaction within the mesoporous ZIF layer, which protects these molecule-sensitive clusters from the complex tumor microenvironment. The host–guest encapsulated rPMo cluster in the ZIF-8 lattice not only endows the nanocomposites with a photothermal conversion property, but also renders them hydrophilic by forming a hydrogen bond network with the surrounding water molecules. This enhances its dispersion in aqueous systems and the delivery of the hydrophilic HSP90 inhibitor epigallocatechin gallate (EGCG). The tumor depth can be assessed by the ratiometric fluorescence of nanocomposites based on the wavelength-dependent attenuation of biological tissues, which is used to customize the irradiation prescription to induce a sufficient eigen temperature (E.T.) change and release effective amounts of EGCG. Finally, this strategy is successfully applied in vivo on mice bearing two orthotopic tumors at different depths.

2. Results

2.1. Construction of Multichannel Ln-ZIF⊂rPMo Nanocomposites

A multichannel nanocomposite was composed of two main parts: a core–shell $NaLuF_4$:Yb,Er,Tm@$NaLuF_4$ nanophosphor prepared by solvothermal method (Figure S1, Supporting Information) and a rPMo-encapsulated ZIF-8 shell (**Figure 1A**). It showed a spherical morphology with a highly crystallized core and ≈3 nm amorphous shell (Figure 1B; Figure S2, Supporting Information). Elemental scanning indicated that the shell contained Zn and Mo (Figure 1C), corresponding to the ZIF-8 (Zn $(C_4H_6N_2)_n$) and encapsulated rPMo clusters ($PMo^{VI}_8Mo^{V}_4O_{40}^{7-}$), respectively. Since the rPMo clusters (≈10 Å) fit into the lattice of ZIF-8 (≈12 Å) but are significantly larger than the window (≈4 Å), they can be stably trapped in the ZIF-8 layer by host–guest interactions without any noticeable leakage (Figure S3, Supporting Information) and are also protected from the complex tumor microenvironment (Figure S4, Supporting Information). Therefore, it should be both physically and chemically stable for bioapplications.

Due to the encapsulation of rPMo, the nanocomposite exhibited strong absorption in the near-infrared (NIR) spectral region (Figure 1D), which can convert the photoenergy into heat (Figure S5, Supporting Information). Compared with the free rPMo, the Ln-ZIF⊂rPMo possessed better photothermal conversion performance, which is contributed to the aggregation of rPMo in the Ln-ZIF host. It also emitted thermosensitive fluorescence in the green spectral region (Er^{3+}: $^2H_{11/2}\rightarrow{}^4I_{15/2}$ and $^4S_{3/2}\rightarrow{}^4I_{15/2}$), as well as three others in the red (Tm^{3+}: $^1G_4\rightarrow{}^3F_4$ and Er^{3+}: $^4F_{9/2}\rightarrow{}^4I_{15/2}$) and NIR spectral region (Tm^{3+}: $^3H_4\rightarrow{}^3H_6$). These emissions were useful to monitor the E.T. of the nanocomposites during the photothermal conversion process (I_{525}/I_{545}) and to assess the tumor depth (I_{RED}/I_{NIR}), respectively. The thermal response capability of Ln-ZIF⊂rPMo was not affected by the shell coating and was comparable to the bare nanoparticles (Figure S6, Supporting Information). Notably, the energy of ZIF⊂rPMo during water penetration is lower than that of the original ZIF-8, thus allowing more water molecules in its lattice, especially surrounding the guest (Figure 1E). This can be explained by the hydrogen bond affinity of rPMo, which formed a continuous hydrogen bonding network with the surrounding water molecules and promoted their mobility.[26] Therefore, the highly polarized rPMo clusters facilitated aqueous diffusion, counteracted the water repulsion of the hydrophobic ZIF-8, and enhanced the hydrophilicity of the nanocomposites (Figure S7, Supporting Information).

Notably, the hydrogen bond network formed by rPMo clusters not only enabled the dispersion of hydrophobic ZIF-8-coated nanocomposites in aqueous solution, but also benefited hydrophilic drug delivery. Due to the strong hydrophobicity, hydrophilic drug molecules are difficult to load on ZIF-8 and are rapidly released in aqueous solutions, which prevents controlled drug delivery to the tumors. The conventional strategy is to modify ZIF-8 with hydrophilic or amphiphilic molecules, such as polyethylene glycol (PEG).[27,28] However, although the hydrophilicity is improved after modification, the active sites on the surface capable of adsorbing the drug molecules are reduced, so that the drug is unstably absorbed by weak electrostatic interactions. In contrast, ZIF⊂rPMo not only has the same number of active sites as ZIF-8, but has also improved electrostatic interaction with drug molecules due to the reduced ζ potential (Figure S8, Supporting Information). Meanwhile, it is also able to stably adsorb drug molecules through the hydrogen bond network (**Figure 2A**). For example, the loading amount of EGCG per milligram of Ln-ZIF⊂rPMo (389.8 ± 14.8 μg) was 4.3 times higher

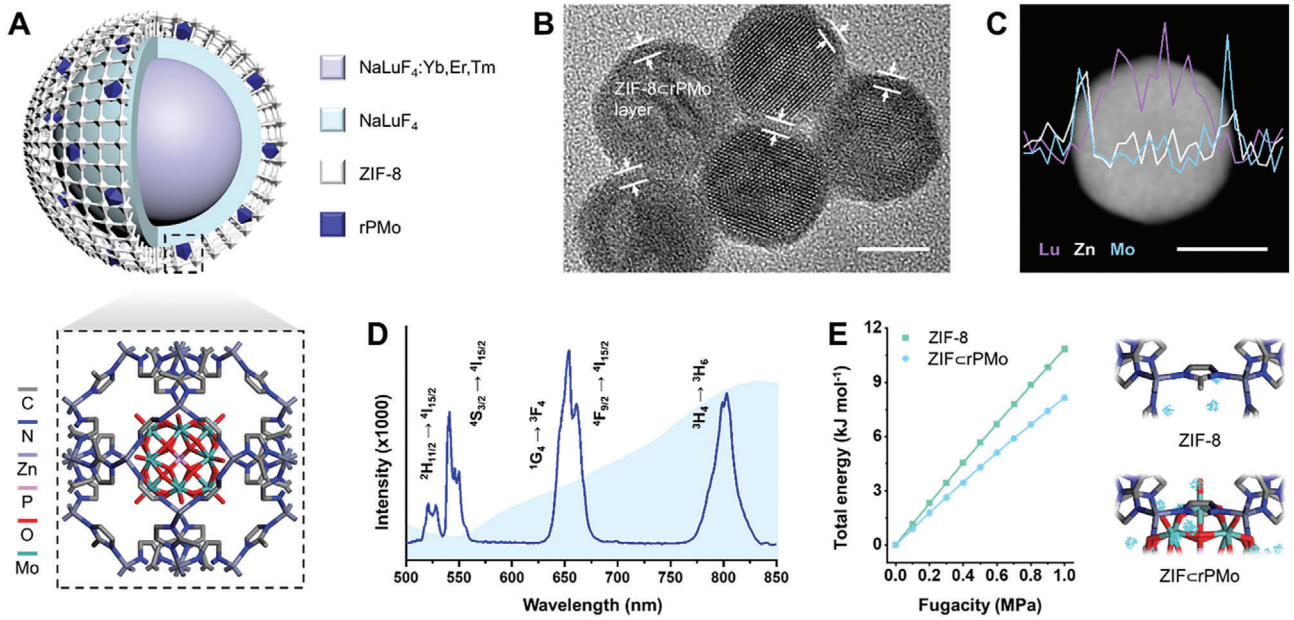

Figure 1. Construction and characterization of Ln-ZIF⊂rPMo. A) Schematic presentation of as-designed Ln-ZIF⊂rPMo (top) and the host–guest assembly of the rPMo cluster in the ZIF-8 lattice (bottom). B) TEM image and C) energy-dispersive X-ray analysis line scan profile of Ln-ZIF⊂rPMo. Scale bar 10 nm. D) Fluorescence spectrum of Ln-ZIF⊂rPMo under 980 nm excitation. The light blue curve showed the absorbance of rPMo cluster. E) Theoretical total energy of ZIF-8 and ZIF⊂rPMo versus fugacity (left) and molecular dynamics simulations (right). For visualization purposes, only part of the lattice is shown. The scale bar is 20 nm.

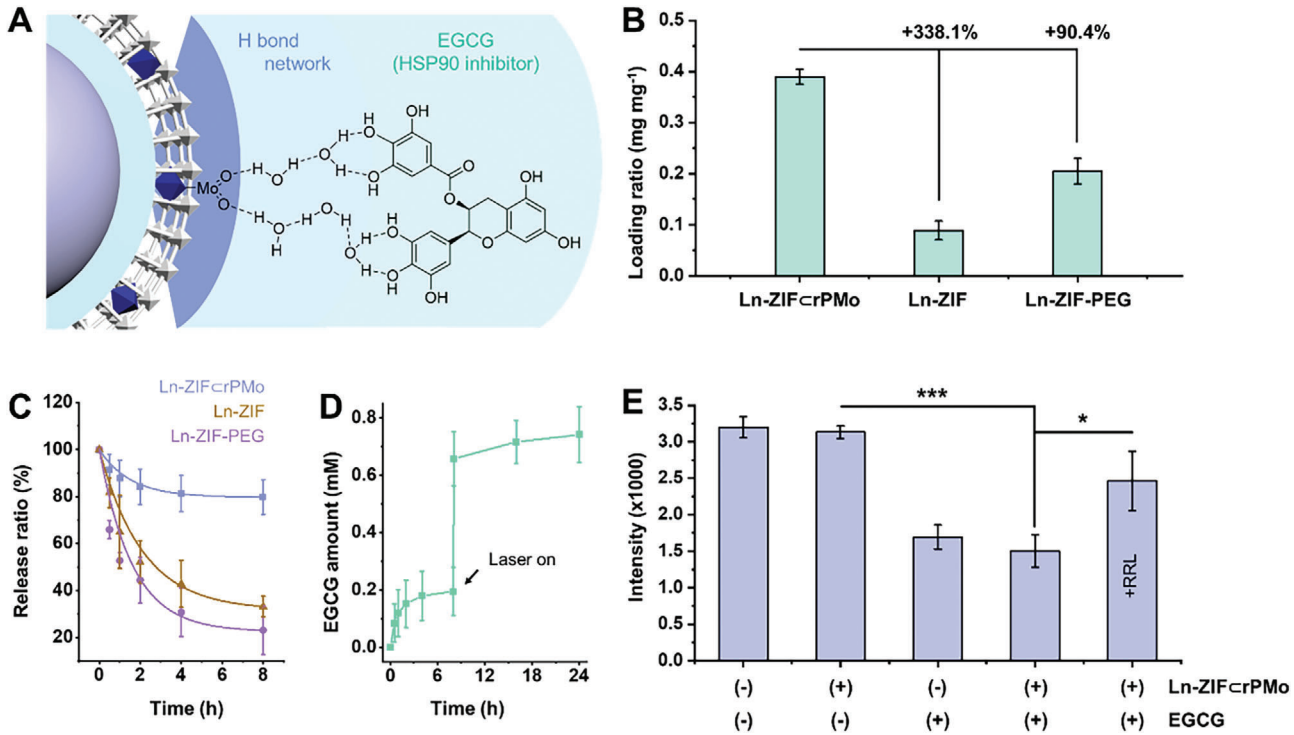

Figure 2. EGCG delivery and release property of Ln-ZIF⊂rPMo. A) Schematic representation of stabilized EGCG loading by formation of a hydrogen bond network by the rPMo clusters. B) Loading ratio of EGCG per milligram of Ln-ZIF⊂rPMo, Ln-ZIF, and Ln-ZIF-PEG. C) Spontaneous release ratio of EGCG from Ln-ZIF⊂rPMo, Ln-ZIF, and Ln-ZIF-PEG versus time. D) Amount of EGCG in the supernatant of Ln-ZIF⊂rPMo-EGCG before and after laser irradiation. E) Relative units studied by luminescence determination of luciferase in saline, Ln-ZIF⊂rPMo, EGCG, and Ln-ZIF⊂rPMo-EGCG. The HSP90-rich rabbit reticulocyte lysate (RRL) was added for recovery study. Statistical significance was determined by one-way t-tests. Data presented as mean ± SD ($n = 3$). *$p < 0.05$ and ***$p < 0.001$.

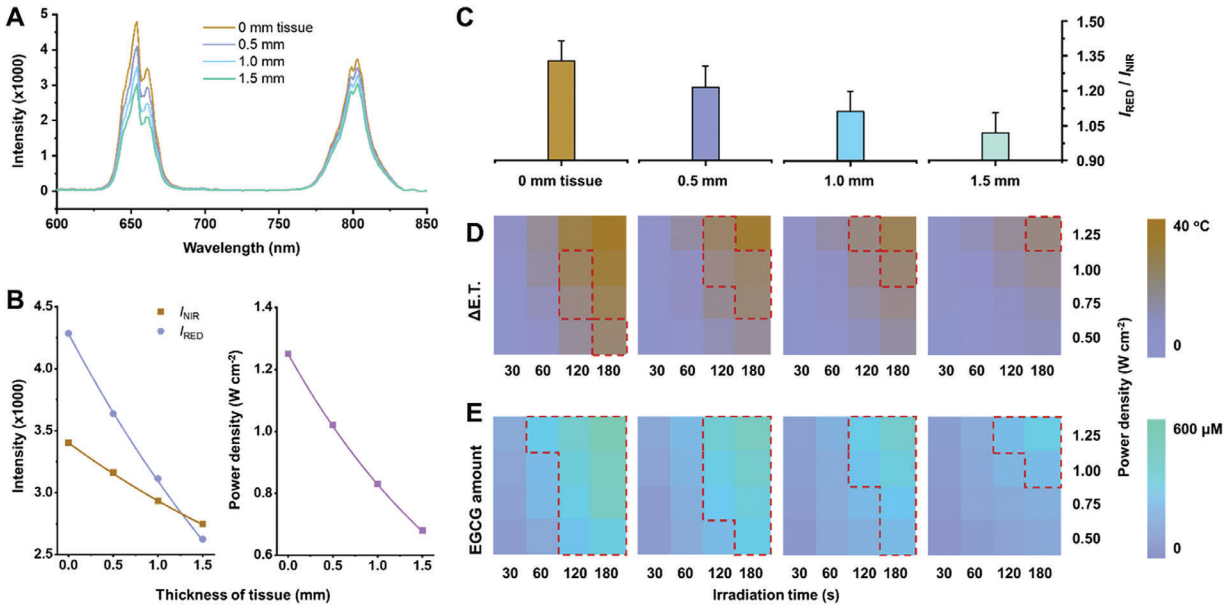

Figure 3. Fluorescence, heat generation, and EGCG release property under different thickness of tissue. A) Fluorescence spectrum of Ln-ZIF⊂rPMo-EGCG and B) fluorescence intensity in the red and NIR spectral region (left) and power density of 808 nm laser (right) under different thickness of tissue. C) I_{RED}/I_{NIR} fluorescence ratio, D) E.T. change (B), and E) amount of released EGCG of Ln-ZIF⊂rPMo-EGCG under different thickness of tissue. The E.T. and drug release amount were measured as a function of laser power density and irradiation time, which was considered as two parameters in the irradiation prescription. E.T. and EGCG amount in the effective range was outlined by a dark red dotted line. Data represented as mean ± SD ($n = 3$).

than that of Ln-ZIF (88.9 ± 18.3 μg), indicating the great influence of hydrophilicity on the delivery of EGCG (Figure 2B; Figures S9 and S10, Supporting Information). Although the conventional Ln-ZIF-PEG loaded more EGCG (204.8 ± 25.1 μg) than Ln-ZIF, it was still significantly lower than Ln-ZIF⊂rPMo, highlighting the importance of the hydrogen bond network in EGCG loading. Furthermore, the EGCG was more stably adsorbed on the Ln-ZIF⊂rPMo due to the hydrogen bond network (Figure 2C). Nevertheless, the hydrogen bonds were still breakable upon heating (18.8 kJ mol^{-1}), which enabled photothermally triggered drug release under laser irradiation (Figure 2D). Under laser irradiation, ≈59.64% of the loaded EGCG can be released from the Ln-ZIF⊂rPMo within 180 s, which follows the Higuchi model and the mechanism for skeleton diffusion (Figure S11, Supporting Information). In contrast, spontaneous release is slow and less influenced by the biological environment and therefore does not lead to significant side effects (Figure S12, Supporting Information). This observation suggests that EGCG is uniformly loaded and released from the inert structure through diffusion. The released EGCG can reach an effective amount (>200 × 10^{-6} M) to bind to the C-terminal adenosine triphosphate-binding region, inhibit dimerization, promote conformation, and interfere with the chaperone function of HSP90.[29] In view of this, the HSP90 inhibitory effect of released EGCG was confirmed by a fluorescence assay based on HSP90 activity on luciferase refolding. The results showed that EGCG, instead of Ln-ZIF⊂rPMo, can effectively inhibit the function of HSP90 (Figure 2E). The fluorescence recovery after adding additional HSP90 further demonstrated the role of EGCG as an HSP90 inhibitor. Notably, the Ln-ZIF⊂rPMo can also be used for effective loading with other typical hydrophilic drugs (e.g., doxorubicin hydrochloride, Figure S13, Supporting Information). In short, multichannel nanocomposites Ln-ZIF⊂rPMo were successfully constructed with increased hydrophilic drug loading amount over the hydrophobic Ln-ZIF and the commonly used Ln-ZIF-PEG.

2.2. Prediction of Therapeutic Effect versus Tumor Depth

Since light scattering and absorption by biological tissues is wavelength dependent, the transmittance of NIR fluorescence is higher than that of red fluorescence (Figure S14, Supporting Information). Therefore, the thickness of biological tissue can be assessed by the ratio of the intensities of two fluorescence peaks at different wavelengths. For example, when the thickness of tissue increases (as a model for thicker tissue or more deep-seated tumors), the lanthanide fluorescence is attenuated in both the red and NIR spectral regions (**Figure 3**A), but the attenuation of the red fluorescence (≈38.7%) was about twice that of the NIR fluorescence (≈19.3%) (Figure 3B). Therefore, the ratio decreases with increasing thickness of tissue (Figure 3C). The NIR excitation light for photothermal treatment also decreases as a function of increasing tissue thickness, so different irradiation prescriptions (laser power density and irradiation time) were required to raise the E.T. of the nanocomposites to the therapeutic temperature range under different thickness of tissue (Figure 3D; Figure S15, Supporting Information). The nanocomposites show sufficient sensitivity for temperature sensing (0.0098 K^{-1}) and low temperature uncertainty (<1 K) in the studied tissue thickness and temperature range (Figure S16, Supporting Information). The same situation can also be observed for the EGCG release (Figure 3E). Therefore, with the knowledge of the fluorescence ratio, it was possible to assess the thickness of tissue and then customize the irradiation prescription to achieve an appropriate

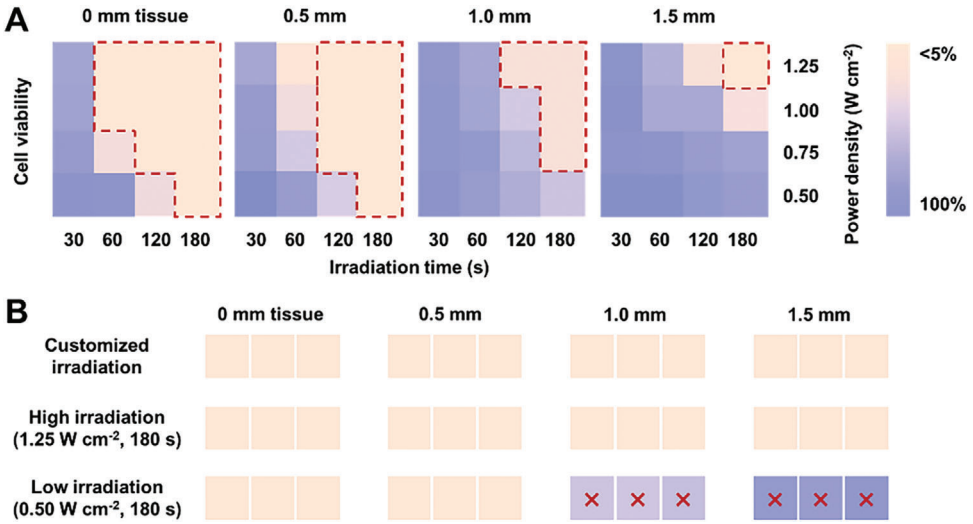

Figure 4. Sensitized photothermal treatment of tumor cells under different thickness of tissue. A) Viability of tumor cells incubated with Ln-ZIF⊂rPMo-EGCG under different thickness of tissue as a function of laser power density and irradiation time (under 808 nm laser irradiation). Tumor cell groups with < 5% viability were highlighted. B) Viability of tumor cells incubated with Ln-ZIF⊂rPMo-EGCG under different thickness of tissue after receiving customized, as well as non-customized high or low irradiation prescriptions. Tumor cell groups with viability > 5% were marked with a red cross.

E.T. and release sufficient EGCG to effectively ablate tumors under different tissue coverage.

Since EGCG increases the cellular sensitivity to hyperthermia, it is expected to allow photothermal treatment at temperatures below the conventional therapeutic range. Therefore, the irradiation prescription for EGCG-sensitized photothermal treatment needs to be optimized to identify the therapeutic temperature range. First, the cell viability versus irradiation prescription under different thickness of tissue was investigated and used as a reference for the following tumor treatment in vivo. As shown in most of the viability diagram, tumor cells can be killed at lower temperature induced by weaker laser power and shorter irradiation time, which confirmed the sensitizing effect of EGCG through HSP90 inhibition (**Figure** 4A; Figure S17, Supporting Information). However, under ≈1.5 mm tissue, only a limited amount of EGCG could be released from the nanocomposites, which was not sufficient to sensitize the tumor cells. Therefore, only the highest irradiation dose was effective in this case. To illustrate the need for customized irradiation prescription for sensitization and treatment, we tested the therapeutic effect of using customized high (1.25 W cm^{-2}, 180 s) and low (0.50 W cm^{-2}, 180 s) irradiation prescriptions and different thickness of tissue (Figure 4B). With 1.0 mm or more tissue, the tumor cells cannot be effectively killed by the low irradiation prescription, in contrast to those receiving customized prescriptions. Notably, although the high irradiation prescription may also result in a high therapeutic effect, it may increase the risk of overtherapy, which we demonstrated in the following in vivo experiments.

2.3. Customized Sensitization and Treatment of Tumors at different Depths

Since the Ln-ZIF⊂rPMo-EGCG is biocompatible, it was then applied to in vivo tumor treatment (Figure S18, Supporting Information). To investigate the performance of customized sensitization and treatment of tumors at different depths, a mouse model bearing two orthotopic tumors was established. Instead of having one deep- and one shallow-seated tumor, both tumors were equally located subcutaneously, while one was covered with a random thickness of tissue (0.5, 1.0, or 1.5 mm) and facilitate accurate measurement of tumor size (**Figure** 5A). Following our previous work, the short-wave infrared (SWIR) intensity of Er^{3+} was used to determine the accumulated amount of Ln-ZIF⊂rPMo-EGCG (Figure S19, Supporting Information). As a reference, a correlation diagram of tumor cell viability, Ln-ZIF⊂rPMo-EGCG amount, and tissue thickness was established, which provided a systematic guide to customize the irradiation prescription (Figure S20, Supporting Information). To further ensure that the photothermal treatment was performed under control, the eigen temperature was monitored by the thermosensitive fluorescence of Ln-ZIF⊂rPMo-EGCG in real time, which allows fine-tuning of the irradiation prescription in response to the actual practice during treatment. After Ln-ZIF⊂rPMo-EGCG injection, the fluorescence ratio was determined to evaluate the thickness of tissue, customize the irradiation prescription, and perform the treatment. 15 d after treatment, the tumors of mice receiving customized irradiation prescription were ablated effectively with ($\Delta V = -54.05 \pm 7.49$ mm^3) or without tissue coverage ($\Delta V = -56.89 \pm 6.25$ mm^3) (Figure 5B; Table S1, Supporting Information). Terminal deoxynucleotidyl transferase dUTP nick end labeling (TUNEL) of tissue sections showed obvious apoptosis of tumor cells and little damage to surrounding tissues in both cases of no tissue and 1.5 mm tissue coverage (Figure 5C). In contrast, the therapeutic effect of the low irradiation prescription on tumors with ($\Delta V = 16.04 \pm 28.16$ mm^3) and without tissue coverage ($\Delta V = -47.88 \pm 5.83$ mm^3) was significantly different; it showed comparable performance in the subcutaneous tumor cases but was unpredictable in the tissue-covered tumor cases (Table S2, Supporting Information). No observable

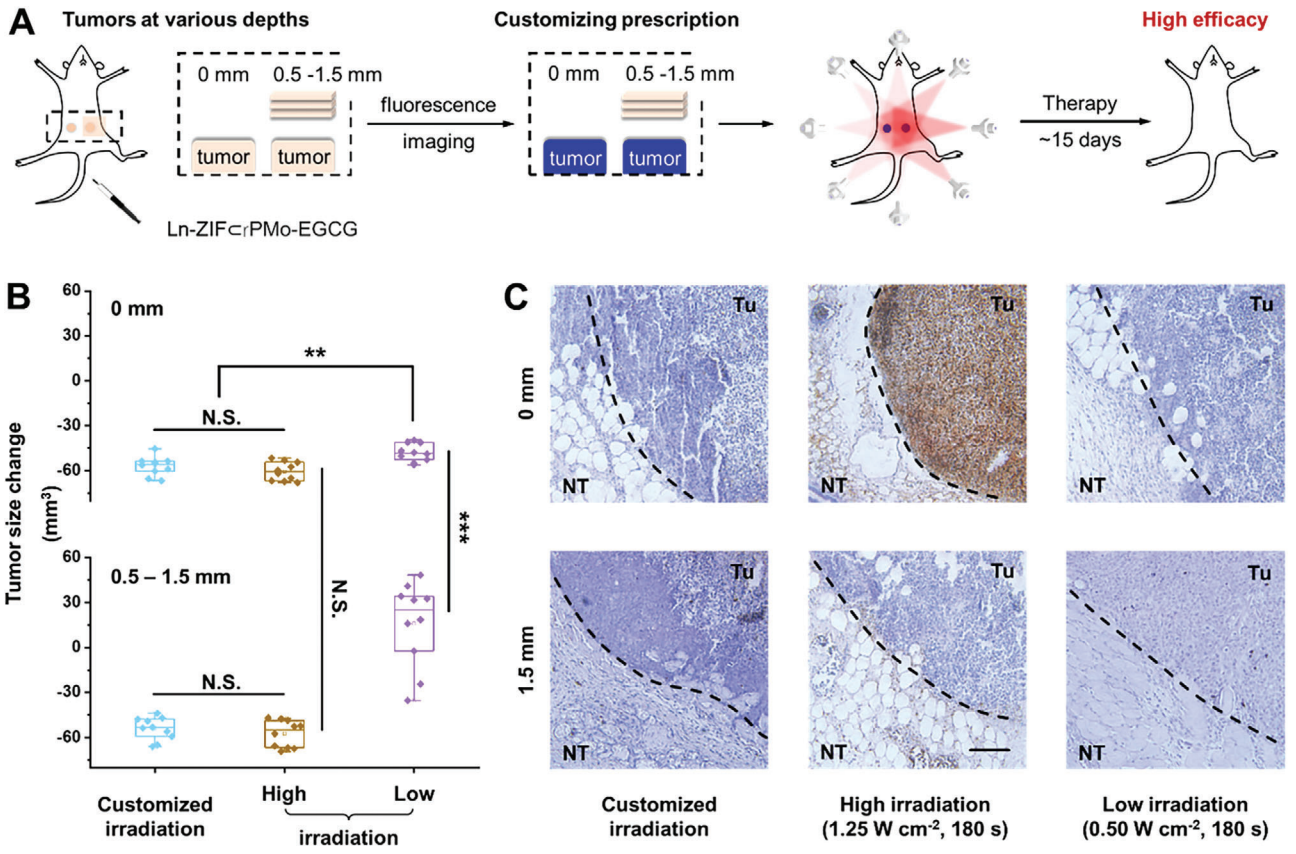

Figure 5. Efficient ablation of tumors at different depths. A) Schematic representation of sensitization and treatment of tumors at different depths using a customized irradiation prescription. B) Change in tumor size of mice after receiving customized, high (1.25 W cm^{-2}, 180 s), or low (0.50 W cm^{-2}, 180 s) irradiation prescriptions. The box range is 25–75%, while the whisker range is 5–95%. The data dots are provided alongside the boxes. C) TUNEL histological sections of the border of tumors (Tu) and normal tissues (NT) collected from a randomly selected mouse from different groups after treatment. The borders are marked by a black dotted line. Statistical significance was determined by one-way *t*-tests. Data presented as mean ± SD ($n = 10$). N.S. is not significant, $^{**}p < 0.01$, and $^{***}p < 0.001$.

apoptosis of cells was found in the TUNEL-stained section of the tumor covered with 1.5 mm tissue. Meanwhile, although those tumors receiving high irradiation prescription were well ablated after the treatment (Table S3, Supporting Information), the tissue sections showed considerable damage to both tumor and surrounding tissues. This is a clear indication of overtherapy and may have a negative impact on postoperative rehabilitation. As a result, the customized irradiation prescription was more successful in treating tumors at unknown depth by our EGCG-sensitized photothermal approach.

3. Discussion

A strategy for customized sensitization and treatment of tumors at different depths was proposed based on a $NaLuF_4$:Yb,Er,Tm@$NaLuF_4$@ZIF-8⊂rPMo-EGCG nanocomposite. The fluorescence of the nanocomposite can indicate the thickness of the covering tissue on the tumor, which allowed the customization of irradiation prescriptions (laser power density and irradiation time). This released sufficient amounts of the HSP90 inhibitor EGCG to sensitize the tumor for photothermal treatment. Tissue thickness and nanoparticle concentration were measured by a Si-based and InGaAs charge-coupled device, respectively, using a 980 nm ring-shaped laser array. The customized irradiation treatment was performed on the same platform using an 808 nm ring-shaped laser array (Figure S21, Supporting Information). After the customized irradiation treatment, the orthotopic tumors covered with different tissue thicknesses were ablated with similarly high efficacy ($\Delta V = -54.05 \pm 7.49$ mm^3 with 0.5–1.5 mm tissue coverage versus $\Delta V = -56.89 \pm 6.25$ mm^3 without tissue coverage), in contrast to those receiving low irradiation ($\Delta V = 16.04 \pm 28.16$ mm^3 with 0.5–1.5 mm tissue coverage versus $\Delta V = -47.88 \pm 5.83$ mm^3 without tissue coverage). Moreover, TUNEL-stained tissue sections showed that the customized treatment resulted in less damage to the surrounding normal tissues compared to the effective but dangerous high irradiation.

In addition to therapeutic applications, this work also contributed to fundamental materials research. We proposed a method to improve the property of widely used ZIF-8 metal–organic framework materials for drug delivery, and confirmed the practicability both experimentally and theoretically. Unlike traditional PEGylation, the ZIF-8⊂rPMo host–guest assembly not only retained as many active sites as ZIF-8, but also formed a hydrogen bond network to stabilize hydrophilic drug molecules. Compared with bare and PEGylated ZIF-8, the ZIF-8⊂rPMo can

deliver more hydrophilic drug molecules (e.g., EGCG) and be more stable, which solves a major issue and beings great opportunities to this class of materials in drug delivery applications. Thus, in the future, this method may be also applicable to other metal–organic frameworks and various applications.

While this work demonstrates the applicability of multichannel nanocomposites to solve the medical dilemma of depth-dependent photothermal ablation efficacy, further efforts are needed: Although sensitized photothermal tumor ablation was realized under 1.5 mm of tissue, the effective therapeutic radius was limited to micro- to millimeters, which can be improved by changing the excitation wavelength (e.g., NIR light in a second biological window or radiofrequency) or constructing an implantable light source. In addition to the light source, the fluorescence wavelength should also be optimized. Due to the wavelength-dependent optical inhomogeneity of biological tissues, the short-wavelength fluorescence as the working emission is more sensitive to changes in tissue thickness but has a shallower penetration depth. Therefore, a balance between sensitivity and penetration depth should be carefully studied regarding the wavelength of working emission to make the fluorescence ratio guidance be accurate and sensitive enough to a larger thickness scale. Moreover, as the fluorescence intensity in the long-wavelength range (>1000 nm) is less affected by tissue thickness, it is a better reference emission than traditional NIR fluorescence, although integration and normalization between different fluorescence spectroscopies would be needed. In addition to wavelength, the intensity of the reference emission can also affect the assessment of tissue thickness (Figure S22, Supporting Information). Therefore, the amounts of fluorescent dopants (e.g., Er^{3+} and Tm^{3+}) can be optimized to tune the sensitivity according to the requirements. In addition, in this work, complex tissue (including skin, fat, muscle, vascular, and connective tissues) was used as an example, and a favorable therapeutic effect was obtained. The optical properties of independent tissues (e.g., skin, muscle, fat) and biofluids (e.g., whole blood) should be carefully studied to gain better knowledge on light penetration to guide further research on the treatment of tumors at different depths. Furthermore, recent work has shown a useful method to assess tissue thickness by deep learning-promoted time-gated imaging, which also motivates us to explore deep learning to enhance the performance of our ratiometric method. To improve drug delivery, in our future work, we will also try to reduce the off-target release of the noncovalently loaded drug molecules (e.g., by using more stable host–guest and coordination interactions).

Supporting Information

Supporting Information is available from the Wiley Online Library or from the author.

Acknowledgements

The authors thank the financial support from the German Federal Ministry of Education and Research (BMBF, 13XP5050A, F.F.L.), the Max-Planck-Fraunhofer collaboration project (Glyco3Display, F.F.L.), the Max Planck Society, EU H2020-MSCA-RISE-2017 Action program (CANCER, 777682, H.Z.), National Natural Science Foundation of China (82001945, X.Z.; 92159103, J.Z.; 22172104, Z.M.), the Joint project of the Beijing Municipal Education Commission and the Beijing Natural Science Foundation (KZ202110028042). Shanghai Pujiang Program (20PJ1410700, X.Z.), NWO Sector Plan for Physics and Chemistry (F.G.M.), and China Scholarship Council scholarship (202008110184, Z.W.). Y.L. personally thanks Prof. Fuyou Li from Fudan University for crucial support and guidance.

Open access funding enabled and organized by Projekt DEAL.

Conflict of Interest

The authors declare no conflict of interest.

Author Contributions

Y.L. conceived the project, analyzed the data and wrote the original manuscript. F.F.L., X.Z., and H.Z. mainly supervised the project, while F.F.L., X.Z., H.Z., J.Z., Z.M, Z.W., and F.G.M. acquired the financial support. Y.L., Z.W., Y.X., Z.M., and X.Z. designed the methodology and established the model for the study. J.Z., Z.M., F.G.M., H.Z., and F.F.L. provided chemical resources. X.Z., H.Z., F.G.M., and F.F.L. provided the characterization resources. J.Z. provided the mice resource. Y.L., Z.W., J.Y.Z., and X.Z. performed the experiments. Y.L., X.Z., F.F.L., and H.Z. decided on the visualization and data presentation. All authors contributed to the reviewing and editing of the manuscript.

Data Availability Statement

The data that support the findings of this study are available in the supplementary material of this article.

Keywords

drug delivery, fluorescent probes, heat shock protein, lanthanide-doped nanoparticles, photothermal therapy

Received: February 27, 2024
Published online: March 28, 2024

[1] W. P. Fan, B. Yung, P. Huang, X. Y. Chen, *Chem. Rev.* **2017**, *117*, 13566.
[2] X. Zhu, W. Feng, J. Chang, Y.-W. Tan, J. Li, M. Chen, Y. Sun, F. Li, *Nat. Commun.* **2016**, *7*, 10437.
[3] X. Zhu, J. Li, X. Qiu, Y.i Liu, W. Feng, F. Li, *Nat. Commun.* **2018**, *9*, 2176.
[4] Z. Xie, T. Fan, J. An, W. Choi, Y. Duo, Y. Ge, B. Zhang, G. Nie, N.i Xie, T. Zheng, Y. Chen, H. Zhang, J. S. Kim, *Chem. Soc. Rev.* **2020**, *49*, 8065.
[5] C. Liang, L. G. Xu, G. S. Song, Z. Liu, *Chem. Soc. Rev.* **2016**, *45*, 6250.
[6] J. Wang, C. Yao, B. Shen, X. Zhu, Y. Li, L. Shi, Y. Zhang, J. Liu, Y. Wang, L. Sun, *Theranostics* **2019**, *9*, 608.
[7] Y. Liu, X. Zhu, Z. Wei, W. Feng, L. Li, L. Ma, F. Li, J. Zhou, *Adv. Mater.* **2021**, *33*, 2008615.
[8] G. C. Li, N. F. Mivechi, G. Weitzel, *Int. J. Hyperthermia* **1995**, *11*, 459.
[9] H.-G. Zhang, K. Mehta, P. Cohen, C. Guha, *Cancer Lett.* **2008**, *271*, 191.
[10] Y. Zhang, S. K. Calderwood, *Int. J. Hyperthermia* **2011**, *27*, 409.
[11] B. Parma, H. Wurdak, P. Ceppi, *Drug Resist. Updates* **2022**, *65*, 100888.
[12] J. Wu, T. Liu, Z. Rios, Q. Mei, X. Lin, S. Cao, *Trends Pharmacol. Sci.* **2017**, *38*, 226.
[13] S. E. Jackson, in *Molecular Chaperones* (Ed: S. Jackson), Springer Berlin Heidelberg, Berlin, Heidelberg **2013**, p. 155.
[14] Y. X. Liu, Z. Wei, X. Q. Liao, J. Zhou, *Acc. Mater. Res.* **2020**, *1*, 225.

[15] Y. X. Liu, Z. Wei, J. Zhou, Z. F. Ma, *Nat. Commun.* **2019**, *10*, 5361.
[16] Z. Wei, T. Cao, L. Li, X. Zhu, J. Zhou, Y. Liu, *Chem. Commun.* **2022**, *58*, 9642.
[17] A. H. All, X. Zeng, D. B. L. Teh, Z. Yi, A. Prasad, T. Ishizuka, N. Thakor, Y. Hiromu, X. Liu, *Adv. Mater.* **2019**, *31*, 1803474.
[18] F. Auzel, *Chem. Rev.* **2004**, *104*, 139.
[19] A. Gnach, T. Lipinski, A. Bednarkiewicz, J. Rybka, J. A. Capobianco, *Chem. Soc. Rev.* **2015**, *44*, 1561.
[20] J. Zhou, Z. Liu, F. Y. Li, *Chem. Soc. Rev.* **2012**, *41*, 1323.
[21] Y. Song, M. Lu, Y. Xie, G. Sun, J. Chen, H. Zhang, X. Liu, F. Zhang, L. Sun, *Adv. Funct. Mater.* **2022**, *32*, 2206802.
[22] Y. Liu, X. Zhu, Z. Wei, K. Wu, J. Zhang, F. G. Mutti, H. Zhang, F. F. Loeffler, J. Zhou, *Angew. Chem. Int. Ed.* **2023**, *62*, 202303570.
[23] J. Xu, W. Han, Z. Cheng, P. Yang, H. Bi, D. Yang, N.a Niu, F. He, S. Gai, J. Lin, *Chem. Sci.* **2018**, *9*, 3233.
[24] J. Xu, W. Han, T. Jia, S. Dong, H. Bi, D. Yang, F. He, Y. Dai, S. Gai, P. Yang, *Chem. Eng. J.* **2018**, *342*, 446.
[25] S. Liu, W. Li, S. Gai, G. Yang, C. Zhong, Y. Dai, F. He, P. Yang, Y. D. Suh, *Biomater. Sci.* **2019**, *7*, 951.
[26] Y. Xu, Y. Liu, H. Han, Z. Ma, *Chem. Mater.* **2022**, *34*, 4242.
[27] H.e Zhang, Q. Zhang, Z. Guo, K. Liang, C. Boyer, J. Liu, Z. Zheng, R. Amal, S. L. J. Yun, Z.i Gu, *J. Colloid Interface Sci.* **2022**, *615*, 517.
[28] X. Chen, Z. Shi, R. Tong, S. Ding, X.u Wang, J. Wu, Q. Lei, W. Fang, *ACS Biomater. Sci. Eng.* **2018**, *4*, 4183.
[29] Y. Li, T. Zhang, Y. Jiang, H.-F. Lee, S. J. Schwartz, D. Sun, *Mol. Pharmaceutics* **2009**, *6*, 1152.